

## Direct Measurements of Fermi Level Pinning at the Surface of Intrinsically n-Type InGaAs Nanowires

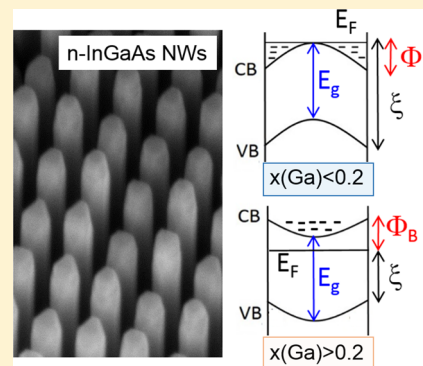
Maximilian Speckbacher,<sup>†</sup> Julian Treu,<sup>†</sup> Thomas J. Whittles,<sup>‡</sup> Wojciech M. Linhart,<sup>‡</sup> Xiaomo Xu,<sup>†</sup> Kai Saller,<sup>†</sup> Vinod R. Dhanak,<sup>‡</sup> Gerhard Abstreiter,<sup>†</sup> Jonathan J. Finley,<sup>†</sup> Tim D. Veal,<sup>\*,‡</sup> and Gregor Koblmüller<sup>\*,†</sup>

<sup>†</sup>Walter Schottky Institut, Physik Department, and Center of Nanotechnology and Nanomaterials, Technische Universität München, Am Coulombwall 4, Garching 85748, Germany

<sup>‡</sup>Stephenson Institute for Renewable Energy and Department of Physics, University of Liverpool, Liverpool L69 7ZF, United Kingdom

### Supporting Information

**ABSTRACT:** Surface effects strongly dominate the intrinsic properties of semiconductor nanowires (NWs), an observation that is commonly attributed to the presence of surface states and their modification of the electronic band structure. Although the effects of the exposed, bare NW surface have been widely studied with respect to charge carrier transport and optical properties, the underlying electronic band structure, Fermi level pinning, and surface band bending profiles are not well explored. Here, we directly and quantitatively assess the Fermi level pinning at the surfaces of composition-tunable, intrinsically n-type InGaAs NWs, as one of the prominent, technologically most relevant NW systems, by using correlated photoluminescence (PL) and X-ray photoemission spectroscopy (XPS). From the PL spectral response, we reveal two dominant radiative recombination pathways, that is, direct near-band edge transitions and red-shifted, spatially indirect transitions induced by surface band bending. The separation of their relative transition energies changes with alloy composition by up to more than  $\sim 40$  meV and represent a direct measure for the amount of surface band bending. We further extract quantitatively the Fermi level to surface valence band maximum separation using XPS, and directly verify a composition-dependent transition from downward to upward band bending (surface electron accumulation to depletion) with increasing Ga-content  $x(\text{Ga})$  at a crossover near  $x(\text{Ga}) \sim 0.2$ . Core level spectra further demonstrate the nature of extrinsic surface states being caused by In-rich suboxides arising from the native oxide layer at the InGaAs NW surface.



**KEYWORDS:** InGaAs nanowires, surface states, Fermi level pinning, photoluminescence, X-ray photoemission spectroscopy

Free-standing semiconductor nanowires (NW) are well known for their prominent surface effects due to their very large surface-to-volume ratio. The presence of surface states, adsorbed impurities, and their charge interactions can massively alter the physical properties of NWs; effects, which can be advantageous or detrimental depending on the given scenario. For example, label-free gas and chemical sensing using semiconductor NW-based electronic devices have been widely demonstrated.<sup>1–4</sup> In this respect, NW materials from low bandgap III–V and metal oxide semiconductors (e.g., InAs, InN, In<sub>2</sub>O<sub>3</sub>, etc.) are particularly attractive due to their exceptional transport properties, straightforward formation of low-resistance Ohmic contacts,<sup>5,6</sup> and very high sensitivity to the adsorption of gaseous or liquid molecules<sup>5,4,7,8</sup> enabled by an intrinsic surface electron accumulation layer present in these materials.<sup>9–12</sup> This unusual surface electronic behavior and electron accumulation in such low-gap materials is commonly attributed to large densities of donor-type surface states, which pin the Fermi level above the conduction band minimum

(CBM) at the surface and thus create strong surface band bending.<sup>9–12</sup>

As much as these surface charge effects are beneficial for sensing devices, that is, the bulk conductivity of the NW can be controlled by surface chemistry, surface states also simultaneously pose various adverse and complex effects for both electronic and optical devices. For example, the electronic properties of InAs NW-field effect transistors (NWFETs) are limited to unipolar device characteristics<sup>5,6,13</sup> (i.e., n-type conduction being dominant), whereas surface states further govern the threshold voltage and on/off ratio of such NWFETs. In addition, the surface states mediated electron accumulation layer also obscures the carrier density in the n-channel and further causes increased charge carrier scattering limiting electron mobilities.<sup>6,14</sup> Surface states are also responsible for

Received: May 20, 2016

Revised: July 8, 2016

Published: July 26, 2016

increased interface state defect densities ( $D_{it}$ ) in InGaAs–NW metal–oxide–semiconductor (MOS)-FETs.<sup>15,16</sup> The situation becomes more complex when the energetic position of the surface defect level changes relative to the band edges as, for example, in band gap tunable III–V semiconductor materials. This can lead also to acceptor-type surface states as in intrinsic GaAs NWs. Although in thick NWs, the surface band bending and consequent depletion of electrons is typically not sufficient to modify the n-type conductive nature in GaAs NWs, the acceptor-type surface states may, however, induce sufficient band bending to produce p-type conductivity when GaAs NWs become very thin.<sup>17</sup> Clearly, these differences in surface space-charge behavior are further expected to play a significant role in future high-mobility InGaAs–NWFETs,<sup>18</sup> where composition-dependent effects of the Fermi level pinning on n- or p-type conductive behavior and contact formation have been completely unexplored.

The band bending induced by surface states is also well known to cause charge separation of excitons, thereby leading to strong increases in nonradiative surface recombination which limit internal quantum efficiencies of optical NW devices.<sup>19–22</sup> There is a large body of recent photoluminescence (PL) investigations of diverse III–V semiconductor NW systems that clearly reveal that native oxide-covered NWs exhibit very strong reduction of PL efficiency due to surface band bending as compared to surface-passivated core–shell NW heterostructures (e.g. GaAs–AlGaAs, GaAs–InGaP, InGaAs–InGaP, InGaAs–InAlAs, and InAs–InAsP core–shell NWs, etc.).<sup>20–24</sup> In addition, nonepitaxial surface passivation schemes using chemical surface treatments (e.g., organic sulfidooctadecylthiol (ODT) passivation or atomic hydrogen cleaning)<sup>25–27</sup> have also been attempted to inhibit surface states while also minimizing strain-induced effects commonly present in epitaxial core–shell NW heterostructures. Furthermore, surface states also induce large built-in electric fields that result in significant shifts of the optical transition energies, as observed in InP NWs.<sup>28</sup>

Despite all the attempts to manipulate surface states and thereby control the surface band bending in traditional III–V semiconductor NWs, a direct and quantitative evaluation of the Fermi level pinning at NW surfaces is still lacking. Instead, to date, the Fermi level pinning has mostly been inferred by comparison to results on flat, planar surfaces. Such comparison is, indeed, difficult and often only indirect, because the dominant sidewall surfaces of III–V-based NWs are mainly composed of {110}-oriented facets, whereas the electronic structure of planar surfaces is most studied for pristine, in situ cleaved {110} orientations or epitaxial {100} orientations.<sup>9,10,29,30</sup> Recently, a few investigations of the surface state density and surface potential were conducted on the {110} sidewall facets of InAs-based NWs using Kelvin probe force microscopy<sup>31</sup> and random telegraph noise spectroscopy in NW-FETs,<sup>32</sup> but the surface band bending has not been quantified.

In order to place the Fermi level pinning effects on a firm footing, it is highly desirable to measure the band bending directly. In this Letter, we therefore employ correlated X-ray photoemission spectroscopy (XPS) and photoluminescence (PL) spectroscopy to quantify the band bending in the technologically important InGaAs NW system. We unambiguously determine the Fermi level to surface conduction band minimum (CBM) separation as a direct measure of the Fermi level pinning at the surface, and further correlate it with the PL

response of intrinsically n-type InGaAs NWs studied comparatively with and without native oxide-covered sidewall surfaces. Importantly, we also delineate the Ga molar fraction (composition dependence) at which flat-band conditions occur, that is, where the surface band bending changes from *downward* bending (electron accumulation) to *upward* bending (electron depletion). Our data is further confirmed by semiquantitative space charge calculations employing solutions of the Poisson equation under the modified Thomas–Fermi approximation. These results are of paramount importance for predicting the nature of intrinsic conduction in InGaAs NWs, estimating Schottky barrier heights for specific contact metals, as well as to control the internal quantum efficiencies in related optical NW devices.

The InGaAs NWs investigated in this study were grown by selective area molecular beam epitaxy (SA-MBE) in a completely catalyst-free growth process.<sup>22,33,34</sup> To enable selective area growth of high-uniformity NW arrays, we employed SiO<sub>2</sub>-covered Si (111) substrates prepatterned with ~80 nm wide openings (pitch of 250 nm) using nanoimprint lithography.<sup>33,34</sup> In total, we realized several InGaAs NW arrays with different alloy composition, that is, a Ga content ranging from  $x(\text{Ga}) = 0$  (pure InAs) to  $x(\text{Ga}) \sim 0.44$ , as determined by high-resolution X-ray diffraction (HR-XRD). For each alloy composition the growth conditions were optimized individually in order to produce high-aspect ratio NWs with high vertical growth yield.<sup>34</sup> Details about the employed growth conditions (V/III flux ratio, growth temperature, etc.) are reported elsewhere.<sup>34</sup> A scanning electron micrograph (SEM) of a typical InGaAs NW array [ $x(\text{Ga}) = 0.12$ ] is exemplified in Figure 1a, illustrating the excellent uniformity and high vertical growth yield. The obtained NWs have a length of  $\sim 950 \pm 20$  nm and diameter of  $\sim 140 \pm 8$  nm, values which are also

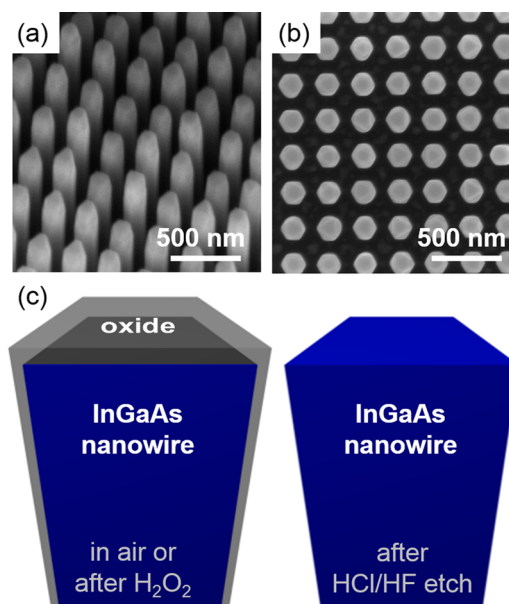


**Figure 1.** SEM images of a representative InGaAs NW array [ $x(\text{Ga}) = 0.12$ ] depicted (a) in tilted view ( $45^\circ$ ) and (b) in top view, illustrating the high uniformity and hexagonal cross-section of the NWs. (c) Schematic illustration of different surface terminations of the as-grown NWs as further employed in detailed photoluminescence experiments; (left) NW surfaces covered by native oxide (when exposed to air or H<sub>2</sub>O<sub>2</sub> treatment); (right) oxide-free NW surfaces after HCl/HF wet chemical etching.

representative for all other investigated samples. The relatively large NW diameter indicates that radial quantum confinement effects in these NWs are negligible. The SEM image recorded in top view (Figure 1b) further evidence the hexagonal shape of the NWs, where the six sidewall facets correspond to the {110} family of orientations as confirmed by transmission electron microscopy (TEM).<sup>35</sup> TEM investigations further revealed that the In-rich InGaAs NWs grown under the selected conditions crystallize in the predominant wurtzite (WZ) phase with a high number of stacking defects while no extended ZB inclusions are observed.<sup>35</sup>

To evaluate the surface band bending effects of the InGaAs NW arrays, we first describe microphotoluminescence ( $\mu$ PL) experiments performed on NWs with different surface termination. In particular, we investigate (i) NW surfaces covered with native oxides, and (ii) NW surfaces free of oxides (surface-passivated NWs) after wet chemical treatment (see Figure 1c). The two types of NW surfaces are realized using the following procedures: (i) Oxide-terminated NWs are created simply by transfer to ambient environment (native oxide formation in air), as well as by oxidizing agents, for example, exposure to hydrogen peroxide ( $\text{H}_2\text{O}_2$ ) at room-temperature.<sup>36</sup> In the latter case, the NW surface is further neutralized by rinsing in  $\text{H}_2\text{O}$  and purging in  $\text{N}_2$  atmosphere. Thereby, an approximately 1–1.5 nm thick oxide film is created that is stabilized mainly by In-rich oxides<sup>27,37</sup> as well as smaller amounts of Ga and As-oxides, as also verified by X-ray photoemission spectroscopy (XPS) in the present investigation. (ii) Oxide-free NW surfaces, on the other hand, are created by removing the native oxide layer in diluted hydrochloric acid ( $\text{HCl}:\text{H}_2\text{O} = 1:1$ ) for  $\sim 10$  s and a subsequent dip in diluted hydrofluoric acid (HF, 1%). This etching step removes the  $\sim 1$ –1.5 nm thick oxide layer and is a self-terminating process, since InGaAs is inert to HCl and HF.<sup>36</sup> The creation and removal of thin native surface oxide layers can be repeated deliberately, thereby allowing the precise thinning down of the NW to the desired diameter (digital etching process). We note that after the applied  $\text{H}_2\text{O}_2/\text{HCl}/\text{HF}$  procedures the surface morphology of the {110} NW sidewalls remains atomically smooth, as verified by TEM analysis.

A direct comparison of the PL spectral response of oxide-covered NWs and HCl/HF-treated NWs (free of surface oxide) is illustrated in Figure 2a for the case of  $x(\text{Ga}) = 0$  (pure InAs NWs). The PL was recorded at 8 K (excitation power density of  $0.2 \text{ mW}/\mu\text{m}^2$ ), using a 632.5 nm He–Ne laser as excitation source and a liquid-nitrogen-cooled InSb detector.<sup>35</sup> Note that oxide-free surfaces are preserved by placing the passivated NWs into the evacuated liquid-helium-cooled cryostat of the PL setup immediately after the HCl/HF-treatment. The PL response of the oxide-covered NWs (black solid curve) and HF-treated passivated NWs without oxide (red solid curve) exhibit distinctly different features: First, the PL peak intensity increases by a factor of  $\sim 2$  upon removal of the native oxide under the applied HCl/HF-treatment. This signal enhancement suggests that surface states become effectively passivated, thereby suppressing recombination channels from the NW surface, in agreement with previous results obtained for InAs and InP NWs.<sup>26,38,39</sup> We note that the signal enhancement is even stronger ( $>5$ -fold increase of relative PL peak intensity) in thinner InAs NWs ( $\sim 70$ – $80$  nm) (not shown), which is expected due to the more pronounced influence of surface states under increased surface-to-volume ratio. Importantly, the changes in PL efficiency by the manipulation of the surface

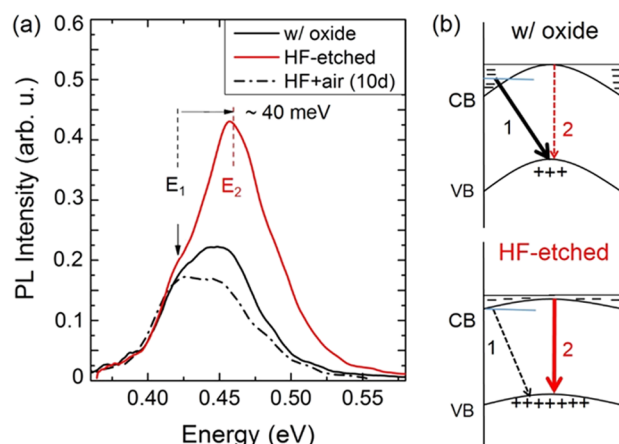


**Figure 2.** (a) Low-temperature (8 K) PL spectra of as-grown NWs covered by surface oxide (black solid curve), after HCl/HF-etching (red solid line), as well as after subsequent 10-day exposure to ambient air (black dashed line). (b) Schematic illustration of the effect of band bending on the PL transitions. High surface state densities lead to strong band bending and electron accumulation at the surface (upper panel), yielding a dominant indirect low-energy transition (labeled 1) between near-surface electrons and holes in the core. Removal of surface states by HF-etching reduces the surface band bending (lower panel), allowing direct band-to-band transition at higher energy (labeled 2) with enhanced quantum efficiency. Note, the band bending is only illustrative here while actual, calculated band bending profiles are shown in the Supporting Information.

oxide layer are, as expected, fully reversible: when transferring the HF-passivated InAs NWs to ambient conditions for  $\sim 10$  days, reoxidation of the NW sidewall surfaces occurs which results in nearly the same PL response as that obtained in the initial case of native oxide-covered NWs (see black dashed curve in Figure 2a).

Second, characteristic differences in the dominant transition energies are noted when comparing oxide-covered/unpassivated NWs (either initially native-oxide covered or reoxidized NWs) with HF-treated NWs. In oxide-covered InAs NWs the PL exhibits both a strong transition at low energy around  $\sim 0.42$  eV (marked as  $E_1$ ) and a transition near  $\sim 0.46$  eV (marked as  $E_2$ ). In contrast, in HF-passivated NWs, the transition at around 0.46 eV clearly dominates. This different behavior can be attributed to a change in the dominant recombination mechanism arising from the modified surface band bending under surface passivation, as illustrated schematically in Figure 2b. When large densities of donor-like surface states are present on InAs (oxide-covered case), strong downward band bending occurs at the surface due to Fermi level pinning,<sup>9,10</sup> which results in spatial separation of electrons at the NW surface (electron accumulation) and holes in the center of the NW. The surface band bending thus favors spatially indirect transitions (recombination-type 1) that yield a lower transition energy ( $E_1$ ) as compared to direct transitions (illustrated as recombination-type 2).<sup>28</sup> Simultaneously, the transition probability is also low due to the spatial separation and small overlap of the electron and hole wave functions, which confirms the overall low PL intensity.

In contrast, when surface states are increasingly removed (HF-passivated case), the surface band bending is significantly reduced and thus more direct near band-edge transitions (recombination-type 2) with higher transition probability become favorable. As these transitions occur further away

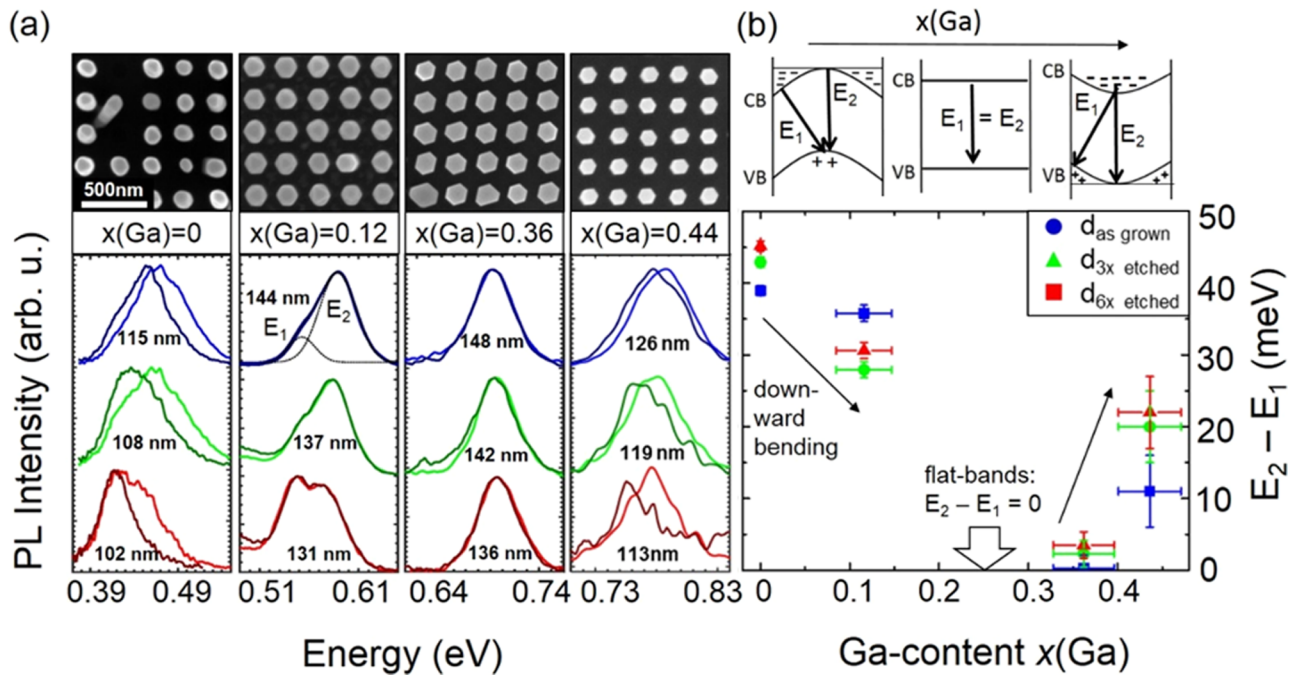


**Figure 3.** (a) Normalized PL spectra as obtained at 8 K and 3.4 mW excitation power for four InGaAs NW samples with different Ga-content, that is,  $x(\text{Ga}) = 0, 0.12, 0.36$ , and  $0.44$ . Dark-colored spectra refer to oxide-covered NWs, whereas bright-colored spectra correspond to HF-passivated NWs, respectively. Representative SEM images of each sample are displayed in the upper panel. PL spectra arranged from top to bottom refer to decreasing NW diameter in increments of  $\Delta d \sim 6\text{--}7$  nm, as a result of the employed digital etching procedure. The decreased NW diameter illustrates the anticipated increase in relative intensity of the low-energy, surface-related transition ( $E_1$ ) with respect to the high-energy, near band-edge transition ( $E_2$ ). (b) Plot of the peak energy difference between  $E_2$  and  $E_1$  as a function of Ga-content  $x(\text{Ga})$ , as obtained for different NW diameters; error bars (vertically) arise from several measurements at different positions and the uncertainty in determining the precise Ga-content (horizontally) due to higher stacking defect frequency toward increased  $x(\text{Ga})$ . The upper panel illustrates the changes in surface band bending and the corresponding indirect ( $E_1$ ) and direct ( $E_2$ ) transitions as a function of Ga-content, which changes from downward to upward bending toward higher  $x(\text{Ga})$ .

from the surface, they proceed at higher energy ( $E_2$ ) and represent more closely the bulk electronic band gap properties of the NW material. This also suggests that previously determined values for the WZ-phase band gap of InAs NWs, as obtained under the presence of native oxides, were slightly underestimated by  $\sim 15\text{--}25$  meV.<sup>35</sup> Although the direct near band-edge transitions are clearly dominant for HF-passivated NWs, still a weak shoulder is present at  $\sim 0.42$  eV, indicating that the band bending is not fully eliminated. However, the contribution of the  $E_1$  transition to the PL intensity is overall very weak, much weaker than the corresponding transition for unpassivated, oxide-covered NWs as obtained from peak fitting. The fact that the energetic position of this low-energy transition does not change markedly, despite the change in band bending, can be explained by the modified strength of the surface confinement potential and the redistribution of electrons and holes. In the case of strong surface band bending, electrons are strongly confined in a quasitriangular quantum well at the surface with their lowest ground state illustrated schematically by the blue line in the upper panel of Figure 2b. When surface band bending is alleviated, electrons are much less confined and simultaneously holes are less localized at the center of the NW (compare lower panel of Figure 2b). The combined effects can lead to indirect transitions with a characteristic energetic position that is very similar to the case for strong downward bending.

The association of the two major recombination processes to indirect surface-related emission ( $E_1$ ) on the one hand and direct near band-edge emission ( $E_2$ ) on the other hand is further substantiated by excitation power-dependent PL

experiments (see Supporting Information). Essentially, excitation power dependent measurements reveal that for the low-energy surface-mediated transition ( $E_1$ ) the integrated PL intensity rises only slowly with increasing excitation power ( $I \sim P^k$  with  $k \sim 0.5$ ), while for the high-energy near band-edge transition ( $E_2$ ) the relative increase in PL intensity is faster ( $k \sim 0.7$ ) (Figure S1). The lower slope for the surface-mediated  $E_1$  transition directly verifies the nature of the spatially indirect transitions, that is, the much lower quantum efficiency due to the poor spatial overlap of the separated electron and hole wave functions.

So far, it has been considered that the energetic position of the surface defect level and, hence, the amount of surface band bending in the investigated InAs NWs is fixed relative to the band edges. This situation changes when the band edges are modified as in band gap tunable materials, where substantially different Fermi level pinning characteristics are expected. Such effects are best illustrated in exploring composition-tunable InGaAs NWs when the alloy composition (i.e., Ga-content  $x(\text{Ga})$ ) is varied over relatively wide ranges. Figure 3 shows low-temperature (8 K) PL spectra of oxide-covered/unpassivated NWs (bright colored spectra) as well as HF-passivated NWs (dark colored spectra) for various different alloy compositions [ $0 < x(\text{Ga}) < 0.44$ ]. Corresponding SEM images of the explored InGaAs NW arrays are further illustrated in the upper panel, verifying that all arrays exhibit similar homogeneity and, thus, make direct comparison feasible. For each alloy composition we also present respective PL data for different NW diameters (using the previously described digital etching scheme).

Several interesting features can be observed from Figure 3: First, as in Figure 2 most of the spectra clearly illustrate again the differently dominating recombination pathways when comparing the spectral shape and peak positions of oxide-covered/unpassivated NWs with HF-treated/passivated NWs. Transitions due to surface-mediated recombination appear either as distinct peaks or shoulders on the low-energy part of the spectra ( $E_1$ ) indicative of red-shifted PL, whereas the more direct bulk-related band-edge emission is reflected by blue-shifted emission appearing at higher energy ( $E_2$ ). The plots using normalized PL intensity appropriately visualize the respective peak positions as well as their separation, which in the following allows to estimate the type and degree of band bending and its dependence on alloy composition. In order to differentiate the individual peaks more clearly, we have further varied the NW diameter which influences the competition in the efficiency between the two recombination pathways, that is, increasing the contribution from the low-energy, surface-mediated transition at reduced NW diameters due to the increased surface-to-volume ratio. This is best seen, for example, in the In-rich InGaAs NW arrays with  $x(\text{Ga}) = 0$  and  $x(\text{Ga}) = 0.12$ , where the low-energy peak becomes clearly prominent toward smaller NW diameters, which corroborates that this transition directly stems from the NW surface. We note, however, that for large decreases in NW diameter (i.e.,  $> 6\times$  the applied digital etching cycles) the surface-state related peak appears to remain even under HF-treatment. This suggests that (i) either the oxide layer intentionally created by exposure to  $\text{H}_2\text{O}_2$  is not fully removed during each HCl/HF-etching cycle, inducing a memory-like effect or (ii) intrinsic surface states appear after oxide removal which arise from nonuniformities in the  $\{110\}$  sidewall facets, e.g. crystallographic defects (stacking defects) and step edges. Nevertheless, as we are primarily interested in the relative peak positions between the two recombination pathways the magnitude of the respective peak efficiency does not play a further role.

Most interestingly, when comparing spectra obtained at different alloy composition, the peak separation, that is, the energy difference  $E_2 - E_1$  between the two peaks changes as a function of Ga-content  $x(\text{Ga})$ . As plotted in Figure 3b, we see that the peak separation is as high as  $\sim 35\text{--}45$  meV for pure InAs NWs—in agreement with the data shown in Figure 2—and gradually decreases toward higher  $x(\text{Ga})$ . For InGaAs NWs with  $x(\text{Ga}) = 0.37$  the peak separation is very small yet positive, that is,  $E_2 - E_1 < 5$  meV. The small separation is also reflected by the near-perfect overlap of the PL peaks measured before and after termination of surface states as well as the rather symmetric spectral shape. For even higher Ga-content of  $x(\text{Ga}) = 0.44$ , the peak separation increases further and amounts to  $E_2 - E_1 \sim 10\text{--}20$  meV. The measured peak separation directly reflects the energetic position of accumulated charge carriers at the surface and, thus, provides a measure for the band bending and Fermi level pinning at the NW surface. Specifically, when surface band bending is present (downward or upward bending), surface charge carriers recombine via spatially indirect transitions, which induces finite and positive values of  $E_2 - E_1$  ( $> 0$ ). On the other hand, ideal flat-band conditions, where spatially no indirect transitions occur, are characterized by  $E_2 - E_1 = 0$ . This situation is further schematically illustrated in the upper panel of Figure 3b. Accordingly, the observed decrease and subsequent increase in  $E_2 - E_1$  with rising  $x(\text{Ga})$  suggests that the band bending changes its sign. In particular, we anticipate a transition from

downward bending (Fermi level pinned above the surface CBM, electron accumulation) in In-rich InGaAs NWs ( $0 < x(\text{Ga}) < \sim 0.2$ ) to upward bending (Fermi level pinned in the band gap at the surface, electron depletion) in more Ga-rich InGaAs NWs ( $x(\text{Ga}) > \sim 0.3$ ). This is supported by our XPS data below, semiquantitative space charge calculations by solving the Poisson equation (Supporting Information, Figure S2), as well as previous literature data on planar n-type InGaAs.<sup>40</sup> Accordingly, near flat-band conditions are thus expected in the region of  $\sim 0.2 < x(\text{Ga}) < \sim 0.3$ , as further verified by detailed XPS measurements (Figure 4). We note that although these

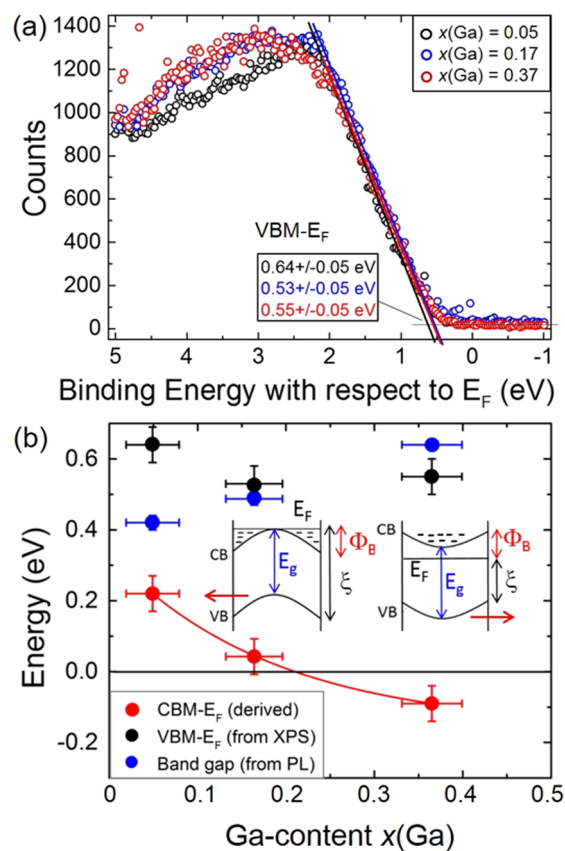


**Figure 4.** (a) Valence band XPS spectra of InGaAs NW arrays with different Ga-content  $x(\text{Ga})$  as recorded near the region of the valence band maximum (VBM) at room temperature in the presence of the native oxide. (b) Evolution of surface VBM to Fermi level separation (black data), band gap energy as determined from PL (blue data), and the barrier height (surface CBM to Fermi level separation, red data) as a function of  $x(\text{Ga})$ ; positive values of barrier height indicate Fermi level pinning within the conduction band (downward bending, electron accumulation), whereas negative values of barrier height corresponds to Fermi level pinning in the band gap (upward bending, electron depletion), as depicted also by the schematics in the inset. The crossover between downward and upward band bending occurs near  $x(\text{Ga}) \sim 0.2$ .

PL-based experiments reproduce closely the expected sign change in surface band bending, the energy difference  $E_2 - E_1$  employed here does not give exactly the Fermi level to surface CBM separation. This is because the ground states of charge carriers populating the near-surface region are confined in quasi-triangular surface quantum wells and the surface potential is screened due to excited charge carriers, which induces slight shifts in the apparent band bending using PL.

To assess the degree of band bending and Fermi level pinning at the surface more quantitatively, we performed X-ray photoemission spectroscopy (XPS) studies on InGaAs NW arrays with alloy compositions in the range of interest. In order to mimic the experimental conditions of the PL measurements as closely as possible, the InGaAs NW arrays were measured in freestanding geometry directly on Si and the NW surfaces were not further cleaned, leaving the desired native oxide behind on the {110}-oriented sidewall planes. The core levels and occupied density of states in the valence band were probed by XPS using a SPECS monochromatic Al  $K\alpha$  X-ray source ( $h\nu = 1486.6$  eV) operating at 200 W and a PSP Vacuum Technology electron-energy analyzer operating with a constant pass energy of 10 eV. Calibration of the spectrometer was performed using a polycrystalline silver foil, cleaned in vacuo by Ar ion sputtering. The Ag  $3d_{5/2}$  photoelectron line had a binding energy (BE) of 368.3 eV and a fwhm of 0.6 eV. The resolution of the XPS is 0.38 eV, as determined from analysis of the Fermi edge of the silver sample.<sup>41</sup> To confirm the existence and composition of the native oxide layer, XPS core level spectra were recorded with data shown in the Supporting Information (Figures S3 and S4). Essentially, we find from analysis of the In 3d, Ga 2p, In 4d, Ga 3d, and As 3d core level peaks that In–O bonds are prevalent and, thus, indium oxide is the dominant oxide with some gallium oxide and arsenic oxide also present in the thin native oxide layer. The proportion of gallium oxide increases in proportion to the Ga-content of the underlying InGaAs NW. These findings of a dominant indium oxide are consistent with previous data obtained from planar InAs.<sup>42</sup>

To gain detailed information on the Fermi level pinning, valence band (VB) photoemission spectra are shown in Figure 4a for three different Ga-contents, that is,  $x(\text{Ga}) = 0.05$ , 0.17 and 0.37, respectively. Here, the relevant energy scale is given with respect to the Fermi level ( $E_F = \text{zero of binding energy}$ ). For each spectrum, the position of the valence band maximum ( $\text{VBM} - E_F = \xi$ ) was determined by extrapolating a linear fit to the leading edge of the VB photoemission.<sup>43</sup> The extracted values for  $\xi$  are in the range of  $\sim 0.53\text{--}0.64 \pm 0.05$  eV, with no distinct dependence on Ga-content  $x(\text{Ga})$  (see also Figure 4b). At first glance, this is somewhat unexpected since with increasing band gap (i.e., increasing  $x(\text{Ga})$ ) the surface VBM usually shifts further away from the Fermi level.<sup>41</sup> Our observation is most likely explained by the peculiar WZ-phase crystal structure with different levels of stacking defects over the In-rich InGaAs NW compositional range,<sup>34,35</sup> which may result in a modification of the effective CB and VB edges. In order to further determine the band bending, we need to take into account the change in band gap ( $E_g$ ) with  $x(\text{Ga})$  and hence the position of the Fermi level also with respect to the surface conduction band minimum ( $\text{CBM} - E_F = \Phi_B$ ). Here, we give the separation between surface CBM and the Fermi level by an effective barrier height  $\Phi_B$ , in analogy to the Schottky barrier height of a metal/semiconductor interface. Because the composition dependence of the WZ-phase band gap of InGaAs NWs has not yet been evaluated theoretically, we employ estimated room-temperature band gap values for each sample as determined from temperature-dependent PL (see Figure 4b).<sup>35,44</sup> For instance, given a band gap of  $E_g \sim 0.42$  eV for WZ-phase InGaAs with Ga-content  $x(\text{Ga}) = 0.05$ , the Fermi level is about  $\Phi_B = 0.22$  eV above the surface CBM, which indicates a downward band bending at the NW surface. As the band gap further increases with  $x(\text{Ga})$ , this lowers the Fermi

level position in the conduction band and ultimately moves it below the CBM at the surface. This results in a transition from downward band bending for high In-content InGaAs NWs ( $\Phi_B > 0$ ) to upward band bending ( $\Phi_B < 0$ ) for higher Ga-content InGaAs NWs, with a crossover ( $\Phi_B = 0$ ) between surface electron accumulation and depletion close to  $x(\text{Ga}) \sim 0.2$  (Figure 4b). This behavior is further illustrated schematically by the corresponding band profiles in the inset, and semi-quantitatively verified by solving the Poisson equation within the modified Thomas–Fermi approximation (Figure S2, Supporting Information). In particular, from these calculations we find that for  $x(\text{Ga}) = 0.05$  the downward bending is as strong as 250 meV, which corresponds to a donor surface state and surface sheet electron density of  $2.5 \times 10^{12} \text{ cm}^{-2}$  for the accumulation layer. When increasing the Ga-content to  $x(\text{Ga}) = 0.17$ , the downward band bending is significantly reduced to 80 meV, giving a surface sheet electron density of  $4.7 \times 10^{11} \text{ cm}^{-2}$ . For  $x(\text{Ga}) = 0.37$ , upward band bending of 50 meV is present, corresponding to an acceptor surface state density of  $2.2 \times 10^{11} \text{ cm}^{-2}$  and an electron depletion layer. We note that these values are estimates based on the assumption of a bulk carrier density of  $1 \times 10^{17} \text{ cm}^{-3}$ , as derived from Seebeck coefficient and NW-field effect transistor measurements of similar NWs. We note that the crossover of  $\Phi_B = 0$  near  $x(\text{Ga}) \sim 0.2$  also closely mimics the composition dependence of Schottky barrier heights as previously measured in Au/n-InGaAs planar diode structures, although these structures were grown along the major (001) planes.<sup>40</sup> Despite this fact, we wish to stress that the flat-band conditions near  $x(\text{Ga}) \sim 0.2$  are not universal in nature for InGaAs-based NWs. On the one hand, freestanding III–V NWs are prone to the stabilization of different crystal phases (WZ versus ZB phase) which alters the electronic band gap<sup>35,44</sup> and, thus, is expected to modify the resulting composition dependence of the effective barrier height. On the other hand, the large tunability of NW diameter may also yield strong radial quantum confinement in low-band gap InGaAs NWs (i.e., for diameters well below the sub-100 nm range<sup>45</sup>), which in future investigations may provide new insights into modified barrier heights in the limit of ultrathin InGaAs NWs.

In conclusion, we investigated the composition dependence of Fermi level pinning at the surface and associated band bending effects in intrinsically n-type InGaAs NWs using correlated XPS and PL spectroscopy. Comparison of the PL response of InGaAs NWs with and without the inherent native oxide reveals the existence two dominant radiative recombination pathways, direct near-band edge recombination and spatially indirect surface-state mediated recombination due to band bending and charge carrier accumulation/depletion at the NW surface. The energetic difference between the two radiative transitions changes significantly with composition, i.e., the difference becoming smaller close to flat-band conditions. The band bending was further directly measured using XPS, revealing a clear transition from downward band bending/surface electron accumulation for high In-content InGaAs NWs (Fermi level pinned above the surface CBM) to upward band bending/surface electron depletion for higher Ga-content InGaAs NWs (Fermi level pinned in the band gap at the surface), with a crossover occurring close to  $x(\text{Ga}) \sim 0.2$ . These results provide very useful information for predicting the intrinsic conduction in InGaAs NWs, for selecting proper contacts to NWs and estimating the respective Schottky barrier

heights, as well as for controlling internal quantum efficiencies in InGaAs NW-based optical devices.

## ■ ASSOCIATED CONTENT

### Supporting Information

The Supporting Information is available free of charge on the ACS Publications website at DOI: [10.1021/acs.nanolett.6b02061](https://doi.org/10.1021/acs.nanolett.6b02061).

Detailed information on excitation power dependent photoluminescence, calculations of the surface charge profiles using solutions of the Poisson equation, and X-ray photoemission spectroscopy core level spectra. (PDF)

## ■ AUTHOR INFORMATION

### Corresponding Authors

\*E-mail: [T.Veal@liverpool.ac.uk](mailto:T.Veal@liverpool.ac.uk).

\*E-mail: [Gregor.Koblmueeller@wsi.tum.de](mailto:Gregor.Koblmueeller@wsi.tum.de).

### Author Contributions

(M.S. and J.T.) These authors contributed equally to this work.

### Notes

The authors declare no competing financial interest.

## ■ ACKNOWLEDGMENTS

The authors thank M. Bichler and H. Riedl for technical support during molecular beam epitaxy growth. This work was funded by the DFG excellence program Nanosystems Initiative Munich (NIM), the collaborative research center SFB 631, and the Technische Universität München, Institute for Advanced Study, funded by the German Excellence Initiative. T.J.W. acknowledges funding from the Engineering and Physical Sciences Research Council, U.K. (EPSRC) (Grant No. EP/J500471/1). W.M.L. and T.D.V. acknowledge EPSRC funding (Grant No. EP/G004447/2).

## ■ REFERENCES

- Cui, Y.; Wei, Q.; Park, H.; Lieber, C. M. *Science* **2001**, *293*, 1289.
- Kolmakov, A.; Zhang, Y.; Cheng, G.; Moskovits, M. *Adv. Mater.* **2003**, *15*, 997.
- Offermans, P.; Crego-Calama, M.; Brongersma, S. H. *Nano Lett.* **2010**, *10*, 2412.
- Du, J.; Liang, D.; Tang, H.; Gao, X. P. A. *Nano Lett.* **2009**, *9*, 4348.
- Thelander, C.; Björk, M. T.; Larsson, M. W.; Hansen, A. E.; Wallenberg, L. R.; Samuelson, L. *Solid State Commun.* **2004**, *131*, 573.
- Ford, A. C.; Ho, J. C.; Chueh, Y.-L.; Tseng, Y.-C.; Fan, Z.; Guo, J.; Bokor, J.; Javey, A. *Nano Lett.* **2009**, *9*, 360.
- Wright, J. S.; Lim, W.; Norton, D. P.; Pearton, S. J.; Ren, F.; Johnson, J. L.; Ural, A. *Semicond. Sci. Technol.* **2010**, *25*, 024002.
- Li, C.; Zhang, D.; Liu, X.; Han, S.; Tang, T.; Han, J.; Zhou, C. *Appl. Phys. Lett.* **2003**, *82*, 1613.
- Noguchi, M.; Hirakawa, K.; Ikoma, T. *Phys. Rev. Lett.* **1991**, *66*, 2243.
- Olsson, L. O.; Andersson, C. B. M.; Hakansson, M. C.; Kanski, J.; Ilver, L.; Karlsson, U. O. *Phys. Rev. Lett.* **1996**, *76*, 3626.
- Mahboob, I.; Veal, T. D.; McConville, C. F.; Lu, H.; Schaff, W. J. *Phys. Rev. Lett.* **2004**, *92*, 036804.
- King, P. C.; Veal, T. D.; Payne, D. J.; Bourlange, A.; Egdell, R. G.; McConville, C. F. *Phys. Rev. Lett.* **2008**, *101*, 116808.
- Dayeh, S. A. *Semicond. Sci. Technol.* **2010**, *25*, 024004.
- Scheffler, M.; Nadj-Perge, S.; Kouwenhoven, L. P.; Borgström, M. T.; Bakkers, E. P. A. M. *J. Appl. Phys.* **2009**, *106*, 124303.
- Si, M.; Gu, J. J.; Wang, X.; Shao, J.; Li, X.; Manfra, M. J.; Gordon, R. G.; Ye, P. *Appl. Phys. Lett.* **2013**, *102*, 093505.
- O'Connor, E.; Brennan, B.; Djara, V.; Cherkaoui, K.; Monaghan, S.; Newcomb, S. B.; Contreras, R.; Milojevic, M.; Hughes, G.; Pemble, M. E.; Wallace, R. M.; Hurley, P. K. *J. Appl. Phys.* **2011**, *109*, 024101.
- Han, N.; Wang, F.; Hou, J. J.; Xiu, F.; Yip, S.-P.; Hui, A. T.; Hung, T. F.; Ho, J. C. *ACS Nano* **2012**, *6*, 4428.
- Tomioka, K.; Yoshimura, M.; Fukui, T. *Nature* **2012**, *488*, 189.
- Demichel, O.; Heiss, M.; Bleuse, J.; Mariette, H.; Fontcuberta i Morral, A. *Appl. Phys. Lett.* **2010**, *97*, 201907.
- Rudolph, D.; Funk, S.; Döblinger, M.; Morkötter, S.; Hertenberger, S.; Schweickert, L.; Becker, J.; Matich, S.; Bichler, M.; Spirkoska, D.; Zardo, I.; Finley, J. J.; Abstreiter, G.; Koblmüller, G. *Nano Lett.* **2013**, *13*, 1522.
- Sun, H.; Ren, F.; Ng, K. W.; Tran, T. T. D.; Li, K.; Chang-Hasnain, C. *ACS Nano* **2014**, *8*, 6833.
- Treu, J.; Stettner, T.; Watzinger, M.; Morkötter, S.; Döblinger, M.; Matich, S.; Saller, K.; Bichler, M.; Abstreiter, G.; Finley, J.; Stangl, J.; Koblmüller, G. *Nano Lett.* **2015**, *15*, 3533.
- Mariani, G.; Scofield, A. C.; Hung, C.-H.; Huffaker, D. L. *Nat. Commun.* **2013**, *6*, 2509.
- Treu, J.; Bormann, M.; Schmeiduch, H.; Döblinger, M.; Morkötter, S.; Matich, S.; Wiecha, P.; Saller, K.; Mayer, B.; Bichler, M.; Amann, M.-C.; Finley, J. J.; Abstreiter, G.; Koblmüller, G. *Nano Lett.* **2013**, *13*, 6070.
- Hang, Q.; Wang, F.; Carpenter, P. D.; Zemlyanov, D.; Zakharov, D.; Stach, E. A.; Buhro, W. E.; Janes, D. B. *Nano Lett.* **2008**, *8*, 49.
- Sun, M. H.; Joyce, H. J.; Gao, Q.; Tan, H. H.; Jagadish, C.; Ning, C. Z. *Nano Lett.* **2012**, *12*, 3378.
- Webb, J. L.; Knutsson, J.; Hjort, M.; Ghalamestani, S. G.; Dick, K. A.; Timm, R.; Mikkelsen, A. *Nano Lett.* **2015**, *15*, 4865.
- van Weert, M. H. M.; Wunnicke, O.; Roest, A. L.; Eijkemans, T. J.; Yu Silov, A.; Haverkort, J. E. M.; 'tHooft, G. W.; Bakkers, E. P. A. M. *Appl. Phys. Lett.* **2006**, *88*, 043109.
- Bell, G. R.; Jones, T. S.; McConville, C. F. *Appl. Phys. Lett.* **1997**, *71*, 3688.
- Karlsson, H. S.; Ghiaia, G.; Karlsson, U. O. *Surf. Sci.* **1998**, *407*, L687.
- Halpern, E.; Elias, G.; Kretinin, A. V.; Shtrikman, H.; Rosenwaks, Y. *Appl. Phys. Lett.* **2012**, *100*, 262105.
- Salfi, J.; Paradiso, N.; Roddaro, S.; Heun, S.; Nair, S. V.; Savelyev, G.; Blumin, M.; Beltram, F.; Ruda, H. E. *ACS Nano* **2011**, *5*, 2191.
- Hertenberger, S.; Funk, S.; Vizbaras, K.; Yadav, A.; Rudolph, D.; Becker, J.; Bolte, S.; Döblinger, M.; Bichler, M.; Scarpa, G.; Lugli, P.; Zardo, I.; Finley, J. J.; Amann, M.-C.; Abstreiter, G.; Koblmüller, G. *Appl. Phys. Lett.* **2012**, *101*, 043116.
- Treu, J.; Speckbacher, M.; Saller, K.; Morkötter, S.; Döblinger, M.; Xu, X.; Riedl, H.; Abstreiter, G.; Finley, J. J.; Koblmüller, G. *Appl. Phys. Lett.* **2016**, *108*, 053110.
- Morkötter, S.; Funk, S.; Liang, M.; Döblinger, M.; Hertenberger, S.; Treu, J.; Rudolph, D.; Yadav, A.; Becker, J.; Bichler, M.; Scarpa, G.; Lugli, P.; Zardo, I.; Finley, J. J.; Abstreiter, G.; Koblmüller, G. *Phys. Rev. B: Condens. Matter Mater. Phys.* **2013**, *87*, 205303.
- DeSalvo, G. C.; Bozada, C. A.; Ebel, J. L.; Look, D. C.; Barrette, J. P.; Cerny, C. L. A.; Dettmer, R. W.; Gillespie, J. K.; Havasy, C. K.; Jenkins, T. J.; Nakano, K.; Pettiford, C. I.; Quach, T. K.; Sewell, J. S.; Via, G. D. *J. Electrochem. Soc.* **1996**, *143*, 3652.
- Timm, R.; Fian, A.; Hjort, M.; Thelander, C.; Lind, E.; Andersen, J. N.; Wernersson, L.-E.; Mikkelsen, A. *Appl. Phys. Lett.* **2010**, *97*, 132904.
- van Vugt, L. K.; Veen, S. J.; Bakkers, E. P. A. M.; Roest, A. L.; Vanmaekelbergh, D. *J. Am. Chem. Soc.* **2005**, *127*, 12357.
- Mattila, M.; Hakkarainen, T.; Lipsanen, H.; Jiang, H.; Kauppinen, E. I. *Appl. Phys. Lett.* **2007**, *90*, 033101.
- Kajiyama, K.; Mizushima, Y.; Sakata, S. *Appl. Phys. Lett.* **1973**, *23*, 458.
- Whittles, T. J.; Burton, L. A.; Skelton, J. M.; Walsh, A.; Veal, T. D.; Dhanak, V. R. *Chem. Mater.* **2016**, *28*, 3718.
- Veal, T. D.; McConville, C. F. *Appl. Phys. Lett.* **2000**, *77*, 1665.

(43) Chambers, S. A.; Droubay, T.; Kaspar, T. C.; Gutowski, M. J. *Vac. Sci. Technol., B: Microelectron. Process. Phenom.* **2004**, *22*, 2205.

(44) Koblmüller, G.; Abstreiter, G. *Phys. Status Solidi RRL* **2014**, *8*, 11–30.

(45) Koblmüller, G.; Vizbaras, K.; Hertenberger, S.; Bolte, S.; Rudolph, D.; Becker, J.; Döblinger, M.; Amann, M.-C.; Finley, J. J.; Abstreiter, G. *Appl. Phys. Lett.* **2012**, *101*, 053103.